Multi-Sampled Grid-Side Current Control for LCL-Filtered VSCs with Enhanced Dissipativity

He, Shan; Yang, Zhiqing; Zhou, Dao; Wang, Xiongfei; De Doncker, Rik W.; Blaabjerg, Frede

Published in:
Proceedings of the 2022 IEEE Energy Conversion Congress and Exposition (ECCE)

DOI (link to publication from Publisher):
10.1109/ECCE50734.2022.9947784

Publication date:
2022

Document Version
Accepted author manuscript, peer reviewed version

Multi-Sampled Grid-Side Current Control for LCL-Filtered VSCs with Enhanced Dissipativity

Shan He
Department of Energy
Aalborg University
Aalborg, Denmark
she@energy.aau.dk

Zhiqing Yang
School of Electrical Engineering and Automation
Hefei University of Technology
Hefei, China
zhiqing.yang@hfut.edu.cn

Dao Zhou
Department of Energy
Aalborg University
Aalborg, Denmark
zda@energy.aau.dk

Xiongfei Wang
Department of Energy
Aalborg University
Aalborg, Denmark
xwa@energy.aau.dk

Rik W. De Doncker
E. ON Energy Research Center
RWTH Aachen University
Aachen, Germany
post_pgs@eonerc.rwth-aachen.de

Frede Blaabjerg
Department of Energy
Aalborg University
Aalborg, Denmark
fbl@energy.aau.dk

***Abstract*—For the grid-side current control of LCL-filtered grid-connected converters, capacitor current active damping is a common method to enhance dissipativity. However, the dissipation near the critical frequency can be jeopardized by the filter parameter deviation, which may result in high-frequency resonances. Besides, the grid voltage feedforward is often abandoned due to the stability consideration, which is however preferred in the practical application to enhance the transient performance. To tackle these challenges, a multi-sampled current control scheme is proposed in this paper. By combining the capacitor current active damping and the capacitor voltage feedforward, not only the dissipative range can be optimized up to the switching frequency, but also the robustness against the filter parameter deviation is enhanced. The validity of the proposed method is verified through the experiments.**

***Keywords*—Multisampling pulse width modulation, dissipativity, robustness, grid-side current control, grid voltage feedforward.**

I. Introduction

Increasing integration of renewables has been regarded as a critical pathway to de-carbonize the power system [1]. As a bridge between the renewables and the power grid, LCL-filtered grid-connected voltage source converters (VSCs) are of importance to fulfill efficient and reliable power conversion [2]. Considering the alternating current controller (ACC) design, a high-bandwidth ACC is required to achieve a fast current regulation [3]. Nevertheless, the control delay affects the bandwidth design of ACC and the VSC-grid interactive stability in the high-frequency range [4], which is the main focus of this paper.

As an extension of the admittance shaping, the passivity-based current control is a promising solution to tackle the VSC-grid interactive instability challenge. Besides the ACC should being stable, the real part of VSC output admittance should be non-negative for all frequencies [5]. However, the pure passivity is impossible to obtain, and the upper boundary of the dissipative region is set to the Nyquist frequency [6]. Consequently, the system stable operation can be secured regardless of the grid admittance below Nyquist frequency.

This work was supported by the Reliable Power Electronics-Based Power System (REPEPS) project at the Department of Energy, Aalborg University, as a part of the Villum Investigator Program funded by the Villum Foundation.

In terms of the single-loop grid-side current control, a non-dissipative region occurs between the anti-resonant frequency and the critical frequency [7]. Hence, extra damping is required to enhance the dissipativity up to the Nyquist frequency. A negated Euler derivative term is inserted in parallel with the proportional resonant (PR) controller to remove the non-dissipative region [8]. The capacitor current active damping (CCAD) is another effective alternative, and the damping coefficient is derived based on the dissipative characteristic of the VSC output admittance at the critical frequency [9]. Besides, the capacitor voltage feedforward (CVF) can also be considered to achieve dissipation [10].

However, the filter parameter deviation can easily introduce a non-dissipative region near the critical frequency when using the CCAD, where the damping coefficient is replaced by a digital filter [11-12]. However, the anti-resonance frequency of the LCL filter shall be constrained to a specific range, which limits the design of the converter-side inductor and the filter capacitor [8, 10, 11]. In addition, the grid voltage feedforward is often ignored when designing the high-frequency dissipativity, hence the transients during the start-up or grid disturbances cannot be addressed properly [13-14].

To overcome the above challenges, a multi-sampled current control scheme is proposed in this paper which combines the CCAD and the CVF. Considering the filter parameter deviation, the dissipation around the critical frequency is enhanced without extra digital-filter-based compensation and constraints on the anti-resonant frequency. Moreover, the CVF helps to suppress the transient currents during the start-up or grid faults. Finally, the experiments validate the proposed control scheme.

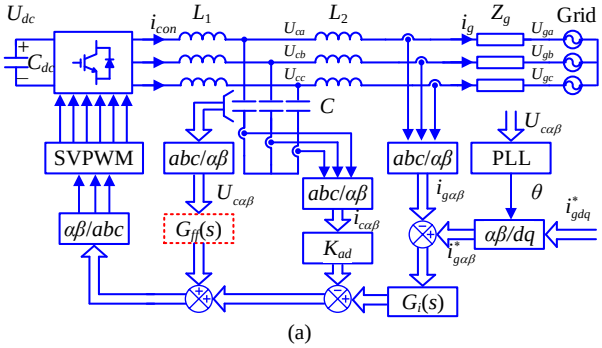

(a)

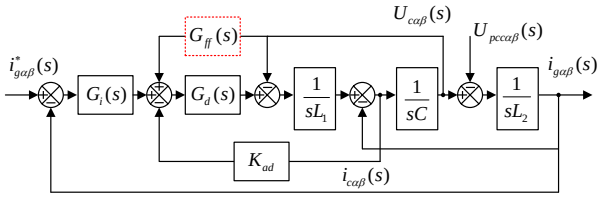

(b)

Fig. 1. Current control diagram of a three-phase grid-connected VSC. (a) Three-phase control diagram, (b) General current control model.

II. Dissipativity Robustness Analysis

A. System model

The investigated three-phase grid-connected VSC with the grid-side current control is illustrated in Fig. 1(a), where U_g is the grid voltage, U_c is the capacitor voltage, U_{dc} is the dc-link voltage, i_{con} is the converter-side current, i_g is the grid-side current, i_c is the capacitor current, and Z_g is the grid impedance. An LCL filter is inserted to suppress the switching harmonics, where L_1 is the converter-side inductance, L_2 is the grid-side inductance, and C is the filter capacitance. According to the general control diagram of the ACC depicted in Fig. 1(b), the grid-side current using the single-loop control is obtained as

$$i_g(s) = G_{cl}(s)i_g^*(s) - Y_o(s)U_{pcc} \tag{1}$$

where $G_{cl}(s)$ is the closed-loop transfer function and $Y_o(s)$ is the VSC output admittance seen from the point of common coupling (PCC). The expression of $G_{cl}(s)$ and $Y_o(s)$ are

$$G_{cl}(s) = \frac{G_i(s)G_d(s)}{s^3L_1L_2C + s(L_1+L_2) + G_i(s)G_d(s)} \tag{2}$$

$$Y_o(s) = \frac{\overbrace{s^2L_1C+1}^{\text{Single-Loop Control}} \overbrace{+sG_d(s)K_{ad}C}^{\text{CCAD}}}{s^3L_1L_2C \underbrace{+s^2L_2CK_{ad}G_d(s)}_{\text{CCAD}} + s(L_1+L_2) + G_i(s)G_d(s)} \tag{3}$$

where K_{ad} is the CCAD coefficient. $G_d(s)$ is the control delay including computation delay and PWM delay, which is

$$G_d(s) = e^{-sT_d}. \tag{4}$$

$G_i(s)$ is the PR controller, which is

$$G_i(s) = K_p + K_r\omega_{rc}\frac{s\cos\varphi_g - \omega_g\sin\varphi_g}{s^2 + \omega_{rc}s + \omega_g^2} \tag{5}$$

where ω_g, ω_{rc}, φ_g, K_p, and K_r represent the grid fundamental angle frequency, the cut-off angle frequency of the resonant controller, the compensation angle of the resonant controller, the proportional and the resonant controller gain, respectively.

B. Single/double-sampling control

According to the passivity-based theory, a grid-connected VSC can be stabilized if the following two constraints are satisfied. First, the closed-loop transfer function in (2) should be stable, which can be achieved through the bandwidth design in [9]. Second, the phase of $Y_o(s)$ should be within $[-90^\circ, 90^\circ]$, i.e., the real part of $Y_o(j\omega)$ should be non-negative. Since the control delay mainly affects the dissipation in the high-frequency range, the resonant controller can be temporarily neglected. By substituting '$s=j\omega$' into (3), the real part of the VSC output admittance is obtained as

$$\mathrm{Re}\{Y_o(j\omega)\} \approx \frac{\overbrace{(1-L_1C\omega^2)K_p\cos(\omega T_d)}^{\text{Single-loop control}} \overbrace{+K_{ad}\omega^2L_1C\cos(\omega T_d)}^{\text{CCAD}}}{A^2+B^2}$$
$$\begin{cases} A = -\omega^2K_{ad}L_2C\cos(\omega T_d) + K_p\cos(\omega T_d) \\ B = \omega^3L_1L_2C - \omega^2K_{ad}L_2C\sin(\omega T_d) - \omega(L_1+L_2) + K_p\sin(\omega T_d) \end{cases}. \tag{6}$$

By changing the sign of $\mathrm{Re}\{Y_o(j\omega)\}$ at the critical frequency, the damping coefficient is designed as

$$K_{ad} = K_p\left(1 - \frac{f_{antinorm}^2}{f_{crit}^2}\right) \tag{7}$$

$$f_{anti} = \frac{1}{2\pi}\sqrt{\frac{1}{L_1C}} \tag{8}$$

$$f_{crit} = \frac{1}{4T_d}. \tag{9}$$

where $f_{antinorm}$ denotes the nominal anti-resonant frequency, and f_{crit} denotes the critical frequency. For the single- and double-sampling PWM shown in Fig. 2, the control delay T_d is $1.5T_{sw}$ and $0.75T_{sw}$, where T_{sw} is the switching period.

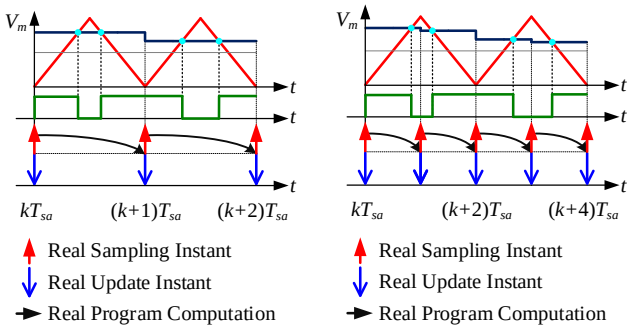

(a) (b)

Fig. 2. Regular sampling PWM. (a) Single-sampling PWM, (b) Double-sampling PWM.

Considering a constant anti-resonant frequency, the non-dissipative boundary using single-sampling PWM is $f_{sw}/6$, while the boundary using the double-sampling PWM is $f_{sw}/3$. Considering a general case of parameter deviations, i.e., $L_1=kL_{1norm}$, $C=kC_{norm}$ where L_{1norm} and C_{norm} are the nominal values of converter-side inductance and filter capacitance, $\mathrm{Re}\{Y_o(j\omega)\}$ can be simplified as

$$\mathrm{Re}\{Y_o(j\omega)\} \approx \frac{K_p\cos(\omega T_d)\left(1-\frac{k^2f^2}{f_{cri}^2}\right)}{A^2+B^2}. \tag{10}$$

According to (8), the non-dissipative region considering filter parameter variation is obtained as

$$f_{non-dissipative} = \left(f_{crit}, \frac{f_{crit}}{k}\right) \text{ or } \left(\frac{f_{crit}}{k}, f_{crit}\right). \tag{11}$$

System specifications of the investigated grid-connected VSC are shown in Table I. Ideally, there are no non-dissipative regions with the nominal filter parameters (k=1), as shown in Fig. 3(a). However, non-dissipative regions are inevitable when the parameter deviation is considered. As presented in Fig. 3(b)-(c), −20% parameter deviation can introduce a larger non-dissipative region than +20% deviation, which can also be explained using (11).

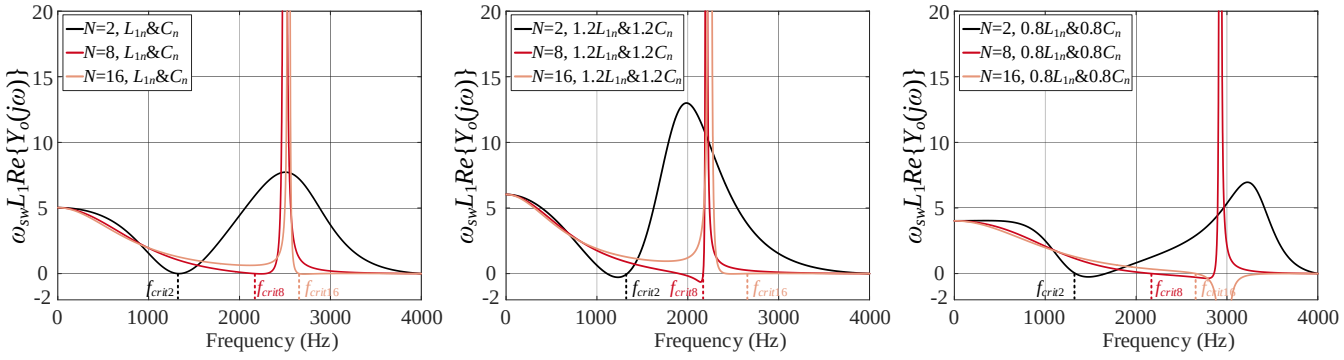

(a) (b) (c)

Fig. 3. Re$\{Y_o(j\omega)\}$ with capacitor current active damping using double-sampling (N=2), eight-sampling (N=8), and sixteen-sampling (N=16). (a) With nominal values of L_1 and C. (b) With a +20% deviation of L_1 and C. (c) With a −20% deviation of L_1 and C.

TABLE I. MAIN PARAMETERS OF GRID-CONNECTED VSC

Symbol	Description	Value	Symbol	Description	Value
P_o	Output power	7 kW	U_g	Grid linevoltage	380 V
U_{dc}	DC-link voltage	700 V	L_1	Converter-side inductance	4 mH
C	Filter capacitance	3 μF	L_2	Grid-side inductance	2 mH
f_{sw}	Switching frequency	4 kHz	N	Sampling rate	2/8/16
f_{anti}	Anti-resonant frequency	1453 Hz	f_r	Resonant frequency	2517 Hz
K_p	Proportional controller gain	20 Ω	K_r	Resonant controller gain	1000 Ω/s
K_{ff}	Proportional feedforward coefficient	0.9	K_{ad2}	Damping coefficient	-3.7 Ω
K_{ad8}	Damping coefficient	11.9 Ω	K_{ad16}	Damping coefficient	15.0 Ω
r_8	Attenuation factor	0.6	r_{16}	Attenuation factor	0.8
L_g	Grid inductive impedance	3 μF	C_g	Grid capacitive impedance	2 mH

C. Multi-sampling control

Multi-sampling PWM is a potential candidate to reduce the control delay [15], and the general multi-sampling PWM is shown in Fig. 4, where the state variable is sampled and the duty cycle is updated multiple times within one switching period. Specifically, the control delay $T_{d,MS}$ is inversely proportional to the sampling rate N [16], which is

$$T_{d,MS} = \underbrace{\frac{1.5}{N}T_{sw}}_{\text{Computation delay + PWM delay}} . \quad (12)$$

Since only two duty cycles are effective within one switching period, based on the voltage-second equivalence, the multi-sampling PWM is equal to a double-sampling PWM with the sampling instant shift and the update instant shift. That is to say, the Nyquist frequency for multi-sampling PWM is equal to the switching frequency [16]. However, to suppress the low-order aliasing caused by the sampled switching harmonics, a modified repetitive filter (MRF) should be inserted in the feedback path [17], as shown in Fig. 5. The MRF contains a compromised moving average filter (CMAF) and a delay compensator, which is given as

$$MRF(s) = \underbrace{\frac{2}{N}\frac{1-e^{-NsT_{sa}}}{1-e^{-2sT_{sa}}}}_{\text{CMAF}}\underbrace{\frac{1-r^N}{1-r^2}\frac{1-r^2e^{-2sT_{sa}}}{1-r^Ne^{-NsT_{sa}}}}_{\text{Delay Compensator}} \approx e^{-\frac{sT_{sw}}{4}} \quad (13)$$

where $r \in (0, 1)$ is the attenuation factor. There is a trade-off between the delay compensation performance and high-frequency noise suppression ability in terms of the variation in r. Consequently, the total loop delay including the control delay and the MRF delay is

$$T_{d,MS-MRF} = \underbrace{\frac{1.5}{N}T_{sw}}_{\text{Computation delay + PWM delay}} + \underbrace{\frac{T_{sw}}{4}}_{\text{MRF delay}} = \frac{6+N}{4N}T_{sw}. \quad (14)$$

Substituting (14) into (9), the critical frequency using multi-sampling control is $\frac{N}{6+N}f_{sw}$. Recalling (11), the non-dissipative region due to the filter parameter deviation is $\left|1-\frac{1}{k}\right| f_{crit}$, multi-sampling control will introduce a wider non-dissipative region than single/double-sampling control when the multi-sampling rate is larger than three. As shown in Fig. 3(c), multi-sampling CCAD cannot enhance the dissipativity although the control delay is reduced.

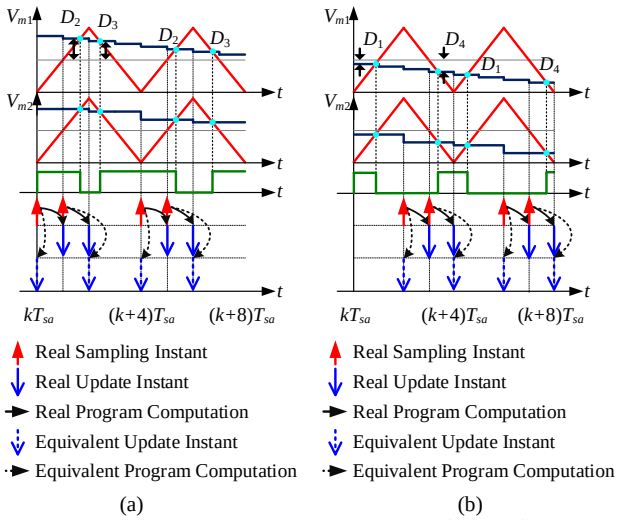

(a) (b)

Fig. 4. General multi-sampling PWM. (a) Positive half cycle of modulation signal, (b) Negative half cycle of modulation signal.

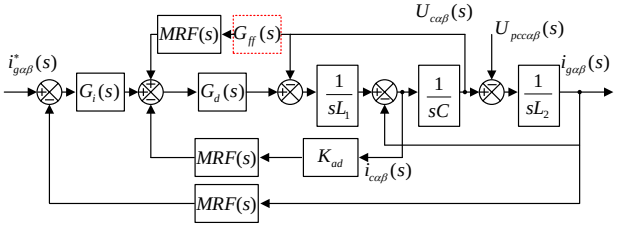

Fig. 5. General multi-sampling PWM. (a) Positive half cycle of modulation signal, (b) Negative half cycle of modulation signal.

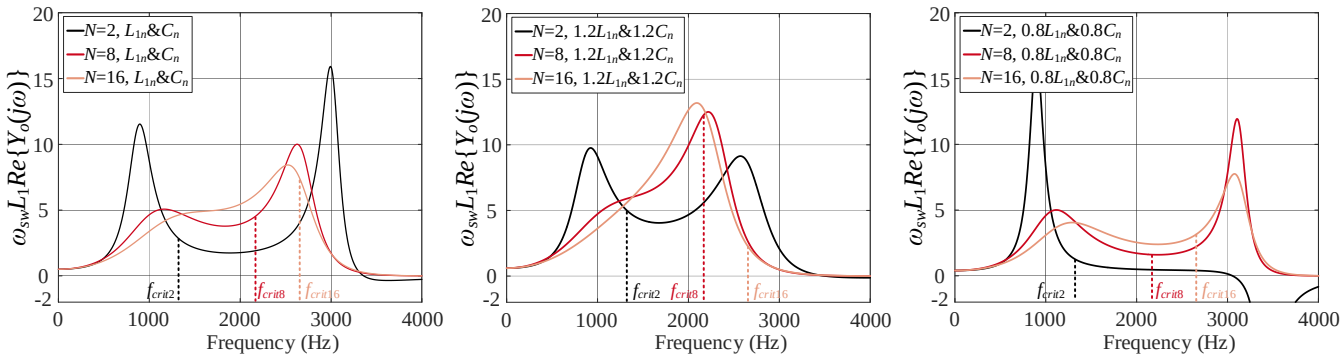

(a) (b) (c)

Fig. 6. Re{$Y_o(j\omega)$} with capacitor current active damping and capacitor voltage feedforward using double-sampling (N=2), eight-sampling (N=8), and sixteen-sampling (N=16). (a) With nominal values of L_1 and C. (b) With a +20% deviation of L_1 and C. (c) With a −20% deviation of L_1 and C.

$$Y_o(s)=\frac{\overbrace{s^2L_1C+1}^{\text{Single-Loop Control}}\ \overbrace{+sG_d(s)K_{ad}C}^{\text{CCAD}}\ \overbrace{-K_{ff}G_d(s)}^{\text{CVF}}}{s^3L_1L_2C+\underbrace{s^2L_2CK_{ad}G_d(s)}_{\text{CCAD}}+s(L_1+L_2)\underbrace{-sL_2K_{ff}G_d(s)}_{\text{CVF}}+G_i(s)G_d(s)}. \tag{16}$$

$$\begin{aligned}\mathrm{Re}\{Y_o(j\omega)\}\approx&\frac{\overbrace{(1-L_1C\omega^2)K_p\cos(\omega T_d)}^{\text{Single-loop control}}\overbrace{+K_{ad}\omega^2L_1C\cos(\omega T_d)}^{\text{CCAD}}\overbrace{-K_{ff}K_p+K_{ff}\omega L_1\sin(\omega T_d)}^{\text{CVF}}}{A^2+B^2}\\ &\begin{cases}A=-\omega^2K_{ad}L_2C\cos(\omega T_d)+K_p\cos(\omega T_d)-\omega K_{ff}L_2\sin(\omega T_d)\\ B=\omega^3L_1L_2C-\omega^2K_{ad}L_2C\sin(\omega T_d)-\omega(L_1+L_2)+K_p\sin(\omega T_d)+\omega K_{ff}L_2\cos(\omega T_d)\end{cases}.\end{aligned} \tag{17}$$

III. Dissipativity Robustness Enhancement

To enhance the dissipativity robustness against the filter parameter deviation and improve the transient performance simultaneously, a proportional CVF term is added in addition to the CCAD. Herein, only a simple proportional feedforward function is used, which is given as

$$G_{ff}(s)=K_{ff} \tag{15}$$

where K_{ff} is the CVF coefficient. After adding the CVF, the VSC output admittance and its real part are given in (16) and (17), respectively. The dissipative characteristic at the critical frequency can be obtained by substituting '$\omega=\omega_{crit}$' into (17), which is given as

$$\mathrm{Re}\{Y_o(j\omega_{crit})\}\approx\frac{2\pi K_{ff}L_1(f_{crit}-f_c)}{A^2+B^2}>0 \tag{18}$$

where $f_c=K_p/(2\pi L_1)$ is the current control bandwidth. Based on (9) and (14), the critical angle frequency ω_{crit} is $0.33\omega_{sw}$ and $\frac{N}{6+N}f_{sw}$ for the double-sampling control and multi-sampling control, respectively. Since f_c is usually set between $0.1f_{sw}$ to $0.2f_{sw}$, Re{$Y_o(j\omega_{crit})$} can always remain positive.

The real parts of the VSC output admittance with both the CCAD and CVF are presented in Fig. 6. As illustrated in Fig. 6(a), the dissipativity near the critical frequency can be enhanced with the CVF. Moreover, as shown in Fig. 6(b)-(c), the VSC output admittance can still behave dissipative around the critical frequency, even with ±20% deviation of L_1 and C. Note that the CVF coefficient should be lower than one to ensure the low-frequency dissipation [18].

However, a non-dissipative region still exists in the higher frequency range for the double-sampling CCAD and CVF. Taking the dissipative characteristic at the switching frequency as an example, Re{$Y_o(j\omega_{sw})$} is given as

$$\mathrm{Re}\{Y_o(j\omega_{sw})\}_{T_d=0.75T_{sw}}\approx\frac{-K_{ff}L_1(\omega_c+\omega_{sw})}{A^2+B^2}<0. \tag{19}$$

Due to the reduced time delay, the dissipative range can be extended up to the switching frequency using multi-sampling. When T_d is $0.5T_{sw}$, Re{$Y_o(j\omega_{sw})$} always remains positive because the CVF coefficient is smaller than one, which is

$$\mathrm{Re}\{Y_o(j\omega_{sw})\}_{T_d=0.5T_{sw}}\approx\frac{K_p(3-K_{ff})}{A^2+B^2}>0. \tag{20}$$

Recalling (14), the multi-sampling control delay is lower than $0.5T_{sw}$ when the sampling rate N is larger than six, and the dissipativity around the switching frequency can be further enhanced.

To summarize, the proposed multi-sampling control scheme with the CCAD and CVF can not only enhance the dissipativity robustness near the critical frequency, but also extend the dissipative range up to the switching frequency. Compared to the methods in [8, 10, 11], there are no constraints to designing the anti-resonant frequency. The dissipation near the critical frequency can still be secured even though the anti-resonant frequency is close to or equal to the critical frequency.

IV. Experimental Results

To further verify the theoretical analysis, experiments are carried out on a three-phase grid-connected VSC with an LCL filter, as shown in Fig. 7. The grid is emulated with a high-fidelity linear amplifier APS 15000. The applied half-bridge module and the control platform are a PEB-SiC-8024 module and a B-BOX RCP control platform from Imperix, respectively. The used current sensor is LEM CKSR 50-P with a bandwidth of 300 kHz. The parameters of the three-phase grid-connected VSC is presented in Table I.

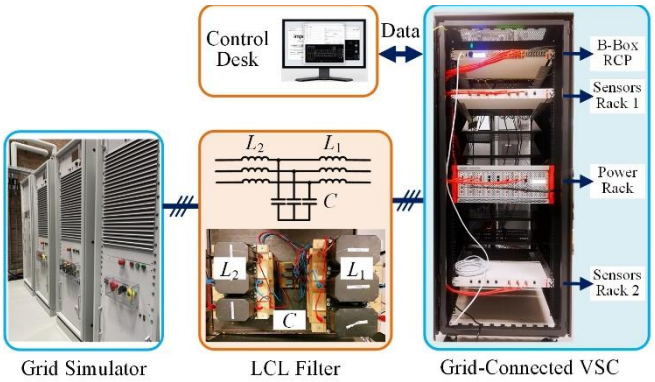

Fig. 7. A down-scaled three-phase grid-connected VSC with an LCL filter.

Bode plots of $Y_o(s)$ and $Y_g(s)$ are depicted in Fig. 8 for various cases. The system can be stabilized with the double-sampling CCAD, considering nominal values of L_1 and C. With a +20% deviation of L_1 and C, $Y_o(s)$ intersects with $Y_g(s)$ in its negative-real-part region, which leads to a -24.4° PM and destabilizes the system. By adding the CVF, the dissipativity near the critical frequency is enhanced. However, the non-dissipative region still exists close to the switching frequency, and the system is destabilized by a -2.6° PM. After implementing the proposed eight-sampling control scheme, the dissipation range can be extended up to the switching frequency and the system is stabilized.

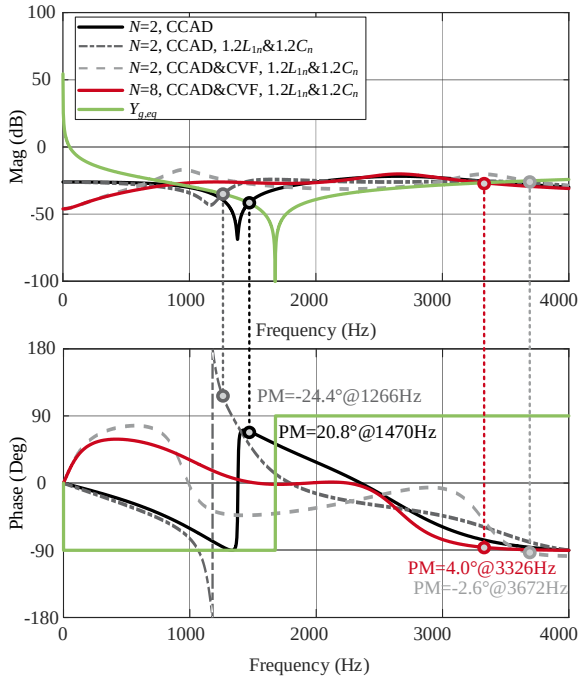

Fig. 8. VSC output admittance seen from PCC $Y_o(s)$ with L_g=3 mH and C_g=3 μF. (CCAD: capacitor current active damping, CVF: capacitor voltage feedforward, N=2: double-sampling, N=8: eight-sampling).

According to the experimental result depicted in Fig. 9(a), the system remains stable with the double-sampling CCAD and the nominal value of L_1 and C. However, the system becomes unstable if a +20% deviation of L_1 and C I considered, as shown in Fig. 9(b). With the additional CVF, the system still loses stability due to the non-dissipative region in the high-frequency range, as illustrated in Fig. 9(c). After implementing the proposed multi-sampling control with the CCAD and CVF, the system can be stabilized even with +20% parameter deviations, as depicted in Fig. 9(d).

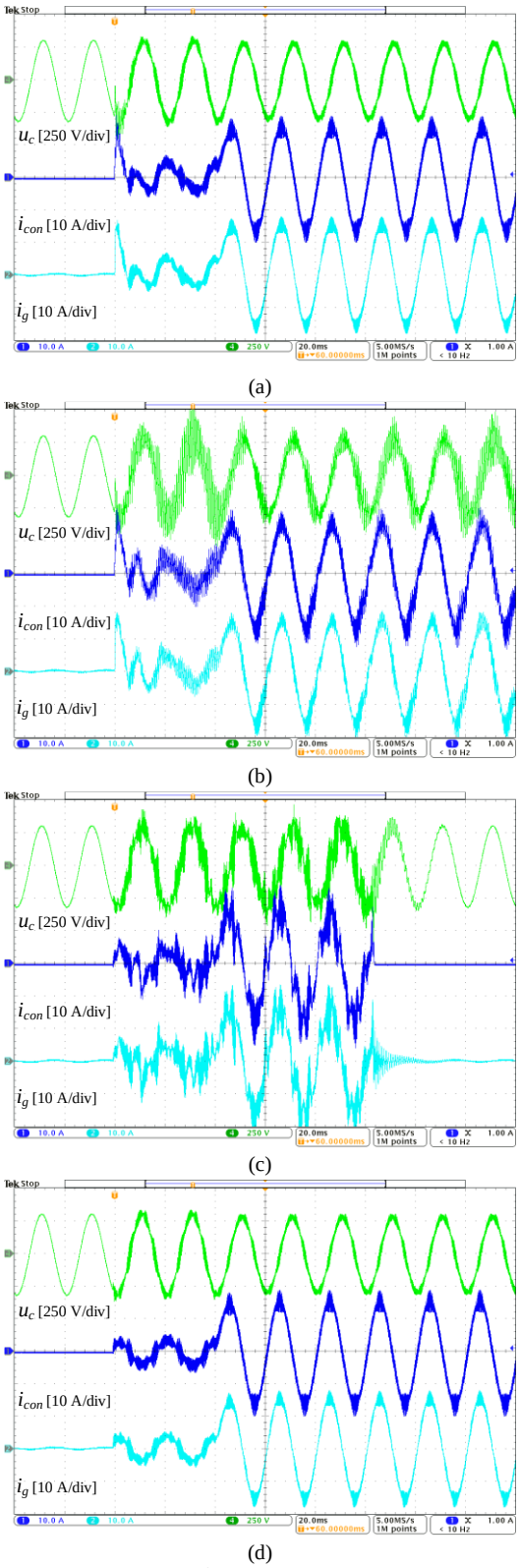

Fig. 9. Experimental results of LCL Filter-I when L_g=3 mH and C_g=3 µF. (a) Double-sampling CCAD with nominal values of L_1 and C. (b) Double-sampling CCAD with +20% deviation of L_1 and C. (c) Double-sampling CCAD and CVF with +20% deviation of L_1 and C. (d) Eight-sampling CCAD and CVF with +20% deviation of L_1 and C.

V. Conclusion

This paper investigates the dissipativity robustness of the CCAD against filter parameter deviations for LCL-filtered grid-following inverters using grid-side current control. The dissipativity near the critical frequency

becomes vulnerable if the filter parameter discrepancy is considered. To tackle this challenge, a multi-sampling control scheme is proposed combining an additional CVF. However, a non-dissipative region is inevitable in the high-frequency area with the double-sampled control. By further utilizing the multi-sampling control, the dissipativity can be enhanced up to the switching frequency, hence wide band resonances can be eliminated and the transient performance is also improved. The effectiveness of the proposed method is validated through the experiment.

REFERENCES

[1] B. Kroposki, B. Johnson, Y. Zhang, V. Gevorgian, P. Denholm, B. Hodge, and B. Hannegan "Achieving a 100% renewable grid: operating electric power systems with extremely high levels of variable renewable energy," *IEEE Power Energy Mag*., vol. 15, no. 2, pp. 61–73, Mar. 2017.

[2] F. Blaabjerg, Y. Yang, D. Yang, and X. Wang, "Distributed power generation systems and protection," *Proc. IEEE*, vol. 105, no. 7, pp. 1311-1331, July 2017.

[3] D. Zhou and F. Blaabjerg, "Bandwidth oriented proportional-integral controller design for back-to-back power converters in DFIG wind turbine system," *IET Renew. Power Gener*., vol. 11, no. 7, pp. 941-951, June 2017.

[4] W. Wu, Y. Liu, Y. He, H. Chung, M. Liserre, and F. Blaabjerg, "Damping methods for resonances caused by LCL-filter-based current-controlled grid-tied power inverters: an overview," *IEEE Trans. Ind. Electron*., vol. 64, no. 9, pp. 7402-7413, Sep. 2017.

[5] Y. Gu, W. Li, and X. He, "Passivity-based control of dc microgrid for self-disciplined stabilization," *IEEE Trans. Power Syst*., vol. 30, no. 5, pp. 2623–2632, Sep. 2015.

[6] L. Harnefors, X. Wang, A. Yepes, and F. Blaabjerg, "Passivity-based stability assessment of grid-connected VSCs-An overview," *IEEE J. Emerg. Sel. Top. Power Electron*., vol. 4, no. 1, pp. 116–125, Mar. 2016.

[7] A. Akhavan, H. Mohammadi, J. Vasquez, and J. Guerrero, "Passivity-based design of plug-and-play current-controlled grid-connected inverters," *IEEE Trans. Power Electron*., vol. 35, no. 2, pp. 2135-2150, Feb. 2020.

[8] X. Wang, F. Blaabjerg, and P. Loh, "Passivity-based stability analysis and damping injection for multiparalleled VSCs with LCL filters," *IEEE Trans. Power Electron*., vol. 32, no. 11, pp. 8922-8935, Nov. 2017.

[9] C. Xie, K. Li, J. Zou, and J. Guerrero, "Passivity-based stabilization of LCL-type grid-connected inverters via a general admittance model," *IEEE Trans. Power Electron*., vol. 35, no. 6, pp. 6636-6648, 2020.

[10] C. Xie, J. Zou, D. Liu, and J. Guerrero "Passivity-based design of grid-side current-controlled LCL-type grid-connected inverters," *IEEE Trans. Power Electron*., vol. 35, no. 9, pp. 9813-9823, 2020.

[11] X. Wang, Y. He, D. Pan, H. Zhang, Y. Ma, and X. Ruan, "Passivity enhancement for LCL-filtered inverter with grid current control and capacitor current active damping," *IEEE Trans. Power Electron*., vol. 37, no. 4, pp. 3801-3812, April 2022.

[12] H. Chen, P. Cheng, X. Wang, and F. Blaabjerg, "A passivity-based stability analysis of the active damping technique in the offshore wind farm applications," *IEEE Trans. Ind. Appl*., vol. 54, no. 5, pp. 5074-5082, Oct. 2018.

[13] S. Zhou, X. Zou, D. Zhu, L. Tong, and Y. Kang, "Improved capacitor voltage feedforward for three-phase LCL-type grid-connected converter to suppress start-up inrush current," *Energies*, vol. 10, no. 5, p. 713, May 2017.

[14] A. Nazib, D. Holmes, and B. McGrath, "Enhanced transient performance of a self-synchronising inverter during start up and severe grid fault conditions," in *Proc. IEEE ECCE Asia*, pp. 1167-1174, March 2021.

[15] S. He, D. Zhou, X. Wang, and F. Blaabjerg, "A review of multi-sampling techniques in power electronics applications," *IEEE Trans. Power Electron*., vol. 37, no. 9, pp. 10514-10533, Sept. 2022.

[16] S. He, D. Zhou, X. Wang, and F. Blaabjerg, "Aliasing suppression of multi-sampled current-controlled LCL-filtered inverters," *IEEE J. Emerg. Sel. Top. Power Electron.*, vol. 10, no. 2, pp. 2411-2423, April 2022.

[17] S. He, D. Zhou, X. Wang, and F. Blaabjerg, "Line voltage sensorless control of grid-connected inverters using multisampling," *IEEE Trans. Power Electron.*, vol. 37, no. 4, pp. 4792-4803, April 2022.

[18] L. Harnefors, L. Zhang, and M. Bongiorno, "Frequency-domain passivity-based current controller design," *IET Power Electron*., vol. 1, no. 4, pp. 455–465, Dec. 2008.